Graphene contacted WS_2/MoS_2 Hybrid Photodetectors with Large Gain Utilizing Interlayer Charge Transfer

*Haijie Tan,[1] Wenshuo Xu, [1] Yuewen Sheng, [1] Chit Siong Lau,[2] Ye Fan, [1] Qu Chen [1] Martin Tweedie [1] Xiaochen Wang, [1] Yingqiu Zhou,[1] Jamie H. Warner[1]**

[1]Department of Materials, University of Oxford, Parks Road, Oxford, OX1 3PH, United Kingdom

2 Institute of Materials Research and Engineering, Agency for Science, Technology and Research (A*STAR), 2 Fusionopolis Way, Innovis, #08-03, Singapore 138634, Republic of Singapore

*Jamie.warner@materials.ox.ac.uk;

Abstract

In this report, we demonstrate how significant improvements in all 2D photodetectors utilizing lateral spaced graphene electrodes can be achieved by exploiting the type II heterostucture in vertically stacked WS_2/MoS_2 semiconducting heterobilayers compared to using homobilayers and monolayer of WS_2 and MoS_2. Photoresponsivity is increased by more than an order of magnitude for the WS_2/MoS_2 heterobilayer compared to homobilayers and two orders of magnitude higher than monolayers of MoS_2/WS_2, reaching 10^3 A/W under an illumination power density of 1.7×10^4 mW/cm^2. The massive improvement in performance is due to the interlayer charge transfer between WS_2 and MoS_2. The efficient charge transfer at the WS_2/MoS_2 heterointerfaces and long trapping time of photo-generated charges contributed to the observed large photoconductive gain over 3×10^4. This approach of making hybrid TMD devices is among the first of its kind to utilize interlayer charge transfer between 2D van der Waals (vdW) crystals for high performing photodetectors.

KEYWORDS: WS_2, MoS_2, interlayer charge transfer, heterostructures, photodetectors

Introduction

Two-dimensional (2D) transition metal dichalcogenides (TMD) have been intensively researched as they provide promising alternatives to conventional semiconductors for future ultrathin electronics and optoelectronics.[1–3] Among them, monolayer MoS_2 and WS_2 have attracted great attention due to their direct bandgaps and high adsorption coefficients.[4] These 2D semiconductors, along with semi-metallic graphene (Gr) and insulating crystals such as hexagonal boron nitride (h-BN) are seen as basic building blocks for a new generation of nano-electronic devices based on 2D vdW crystals.[5] Indeed, many studies have focused on heterostructure optoelectronic devices based on artificially stacked vdW crystals for light-emitting,[6,7] light-harvesting and light-detecting applications. [8–12]

The understanding of interlayer coupling dynamics between 2D materials is essential for better control and design of vdW heterostructure devices. To date, multiple studies have reported the ultrafast interlayer charge transfer between TMDs, which occurs within a picosecond upon photo-excitation at the heterostructured regions.[13,14] This phenomenon is commonly observed in TMD heterostructures with type-II band alignments.[15–18] The charge transfer between TMDs is known to first form layer separated electron-hole pairs with excess energy, or hot excitons, as intermediate states before forming tightly bound excitons. The excess energy leads to a lower binding energy and longer electron-hole pair distance compared with tightly bound excitons,[19] which are conducive for dissociation into free charge carriers and may lead to enhanced photocurrent generation. Moreover, studies on TMD heterostructures reveal that interlayer excitonic lifetimes of heterobilayers are over an order of magnitude larger than intralayer excitonic lifetimes,[15,20] implying a long photocarrier lifetime essential for large photoconductive gain. In this way, artificially designed TMD heterostructure makes a promising option for photodetectors that could outperform monolayer or bilayer TMD crystals by higher light sensitivity.

So far, reports on TMD heterostructures based optoelectronics have focused mainly on vertical architectures with staggered metal contacts sandwiching 2D heterostacks.[6,8,9,21] Less studied are devices with lateral metal-semiconductor-metal (MSM) configuration that involves two or more vdW crystals. This may be due to the difficulty of selective patterning of 2D crystals without damaging its adjacent layer, or the complicated lithography procedures required to overcome it.

In this study, we demonstrate the fabrication of lateral MSM devices based on graphene contacted WS_2/MoS_2 heterostacks and their photoelectrical properties. We develop a process that addresses the aforementioned fabrication challenge by transferring arrays of pre-patterned graphene electrodes and metal bond pads onto arbitrary substrates with pre-transferred TMD domains. The batch transfer of electrodes allows us to fabricate arrays of hybrid TMD device consisting of a WS_2 layer and MoS_2 layer sandwiching graphene electrodes, i.e. a graphene 1D lateral contract to a WS_2/MoS_2 heterostructure. All 2D crystals are grown by chemical vapour deposition (CVD). We conduct spectroscopy analysis of the heterostructures and compare the photoelectrical properties of a lateral Gr-WS_2/MoS_2-Gr device with other TMD monolayer and bilayer devices.

Results and Discussion

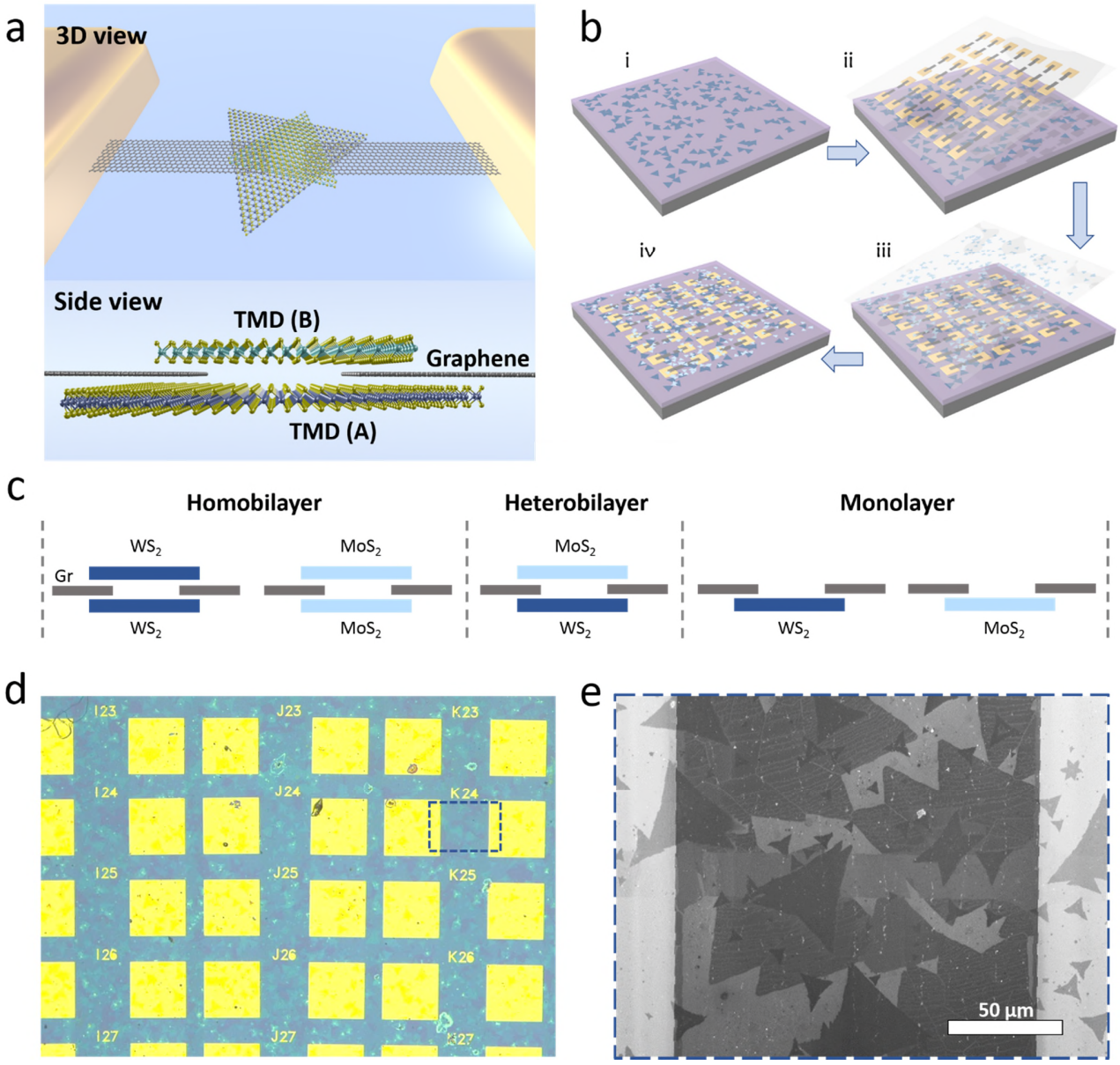

Figure 1. Fabrication schematic and images of hybrid WS_2/MoS_2 photodetector array. (a) Schematic 3D and side views of Gr-WS_2/MoS_2-Gr photodetector. (b) Fabrication process schematic of Gr-TMD-Gr photodetector array. Using PMMA scaffold, pre-patterned Au bond pads and graphene electrodes are transferred onto silicon chip with pre-transferred TMD (A) domains. For bilayer devices, an additional layer of TMD (B) crystals are subsequently transferred onto the same chip. (c) Configuration schematic of the 5 types of photodetectors designed for this experiment, including WS_2/MoS_2 heterobilayer, homobilayer and monolayer of WS_2 and MoS_2. (d) Optical image of a heterobilayer photodetector array consisting of WS_2 and MoS_2 contacted by Gr electrodes. (e) SEM image of framed region (blue dotted line) in (d) showing a hybrid photodetector with MoS_2 and WS_2 domains with graphene contacts.

A perspective schematic of a fabricated bilayer TMD device is shown in Figure 1a. Lateral photodetectors are fabricated with TMD (A)/TMD (B) sandwiching a pair of graphene electrodes. The 2D crystals are transferred using PMMA scaffolds described in the methods section. The TMD bilayer stack bridges a 1 μm gap between the two graphene (source and drain) electrodes, and thus forms a MSM configuration. The main steps for fabricating such a lateral photodetector is shown in Figure 1b. TMD (A) is first transferred onto a silicon chip with a 300 nm oxide layer (Figure 1b, i). On a separate chip, Au bond pads and graphene electrodes are fabricated using electron-beam lithography and oxygen plasma for selective etching. The Au/Gr electrodes are subsequently transferred onto the piece of silicon chip with pre-transferred TMD (A) domains (Figure 1b, ii). For bilayer devices, this is then followed by an additional transfer of TMD (B) to form a TMD bilayer photodetector array (Figure 1b, iii-iv). Our study includes 5 types of devices for comparison, with stacking configurations shown in Figure 1c. Figure 1d is an optical image of one of the fabricated arrays based on WS_2/MoS_2 heterobilayer, and Figure 1e shows an enlarged image of one of the devices consisting WS_2 and MoS_2 domains with graphene electrodes. All the crystals including MoS_2, WS_2 and graphene are synthesized using CVD. The quality and layer number of TMD are further determined using Raman and Photoluminescence (PL) spectroscopy, further described in Supporting Information S1.

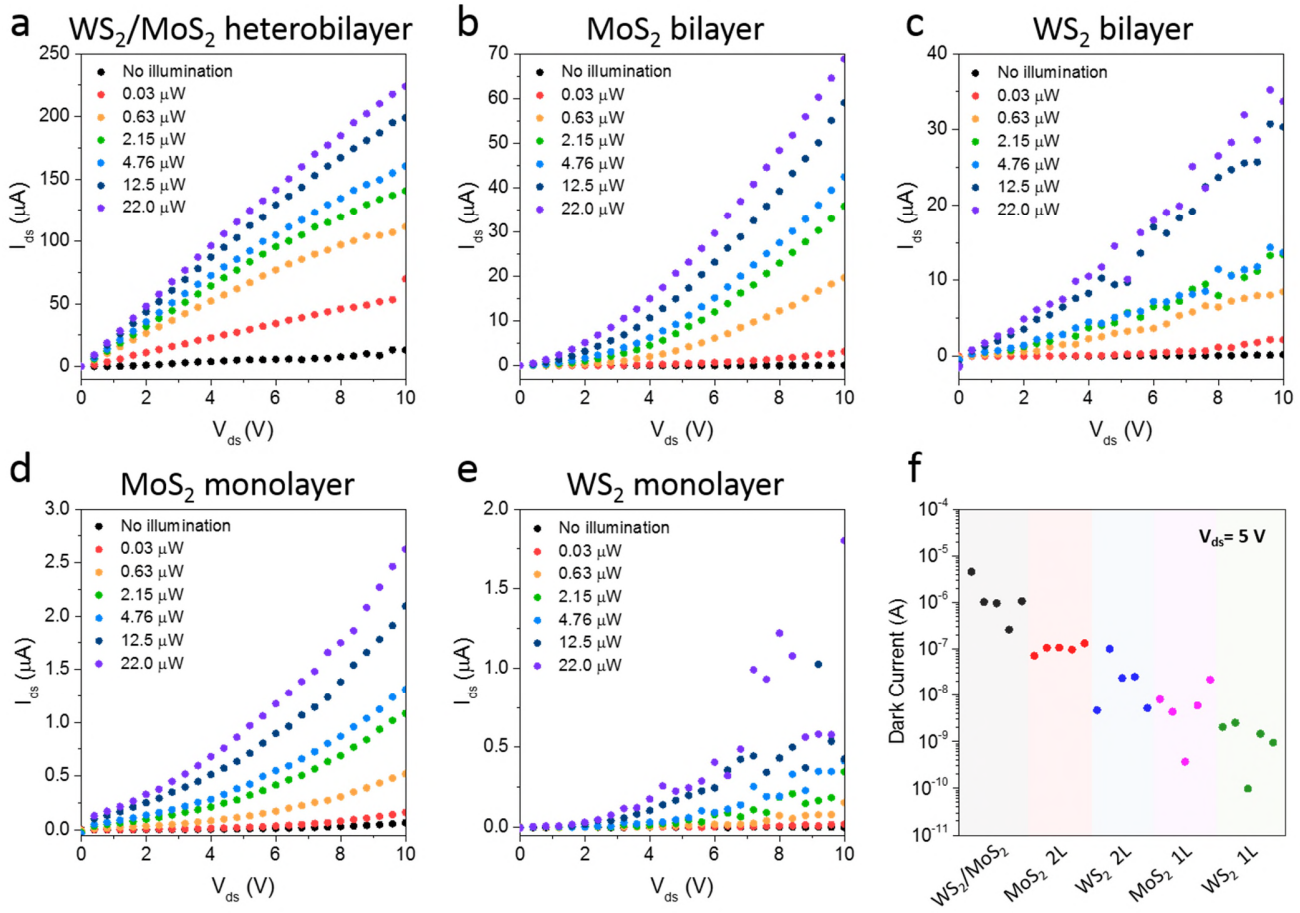

Figure 2. Output characteristics of the 5 types of TMD photodetectors. I_{ds}-V_{ds} measurements under different irradiation power of (a) WS_2/MoS_2 heterobilayer device (b) MoS_2 bilayer device (c) WS_2 bilayer device (d) MoS_2 monolayer device, and (e) WS_2 monolayer device. (f) The distribution of dark current under V_{ds}=5 V of the 5 types of photodetectors.

The output characteristics of the 5 sets of TMD photodetectors under different light irradiation (λ=532 nm) are displayed in Figure 2a-e. All of the photodetectors except for the WS_2/MoS_2 heterobilayer device exhibited a non-linear *I*-*V* curve, indicating a non-ideal contact between the Gr electrodes and the TMD crystals. Under illumination, the WS_2/MoS_2 bilayer device has a near Ohmic characteristics and even showed signs of reaching the saturation region with increasing V_{ds}. The dark current of each types of devices are recorded in Figure 2f, under an applied bias of V_{ds}=5 V. The WS_2/MoS_2 bilayer devices showed the lowest channel resistance with a dark current of ~10^{-6} A. This is followed by MoS_2 bilayer

and WS_2 bilayer devices with dark current ranging from 10^{-9} to 10^{-7} A. The dark current of MoS_2 monolayer (~10^{-8} A) is observed to be slightly larger than WS_2 (10^{-9} A), indicating a lower resistivity of MoS_2 channels compared with WS_2.

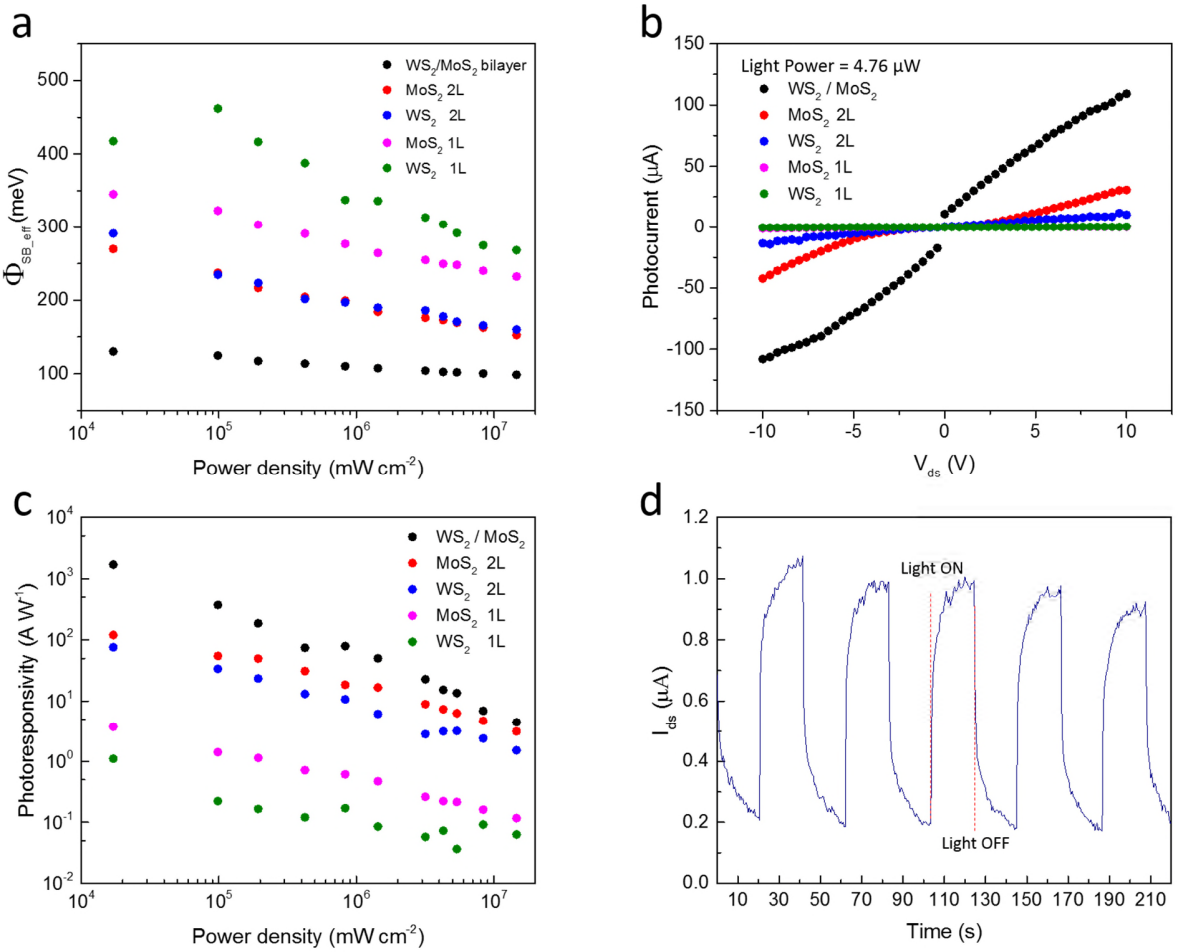

Figure 3. Photoelectrical behavior of TMD photodetectors. (a) Calculated effective Schottky barrier of Gr-TMD interface versus irradiation power density (b) Photocurrent versus V_{ds} under illumination power of 127 μW (c) Photoresponsivity versus irradiation power. (d) Transient photocurrent characteristics of WS_2/MoS_2 heterobilayer device under V_{ds} = +1 V , V_g = -30 V under power density of 1.7×10^4 mW/cm^2.

The photocurrent generation of a photoconductor relies on the change in resistance with differing intensity of incident light. For a lateral photoconductor with a MSM configuration, and especially photodetectors based on 2D crystals, much of the devices' resistance comes from the non-ideal contact, also known as the Schottky contact, formed at the metal-semiconductor interface. The potential barrier (Schottky barrier) inhibits the flow of electrons (holes), allowing limited charge injection through tunneling and thermionic emissions, giving rise to the non-linearity of the output characteristics of the devices. To estimate the effective Schottky barrier height at the Gr-TMD junctions, we introduce a back-to-back Schottky diode model as a simple representation of our MSM photodetectors, and have fitted the *I-V* measurements under different light intensity using a modified thermionic emission equation (Supporting Information S2). Figure 3a shows the obtained effective Schottky barrier height Φ_{SB_eff} versus the incident light intensity of the different devices. We find that Φ_{SB_eff} of all 5 devices have a negative correlation with light power, among which WS_2/MoS_2 bilayer devices exhibited the smallest Φ_{SB_eff} value, reaching below 100 meV under the largest irradiation power. It is also worth noting that the obtained Φ_{SB_eff} corresponds closely with magnitude of current under dark conditions and different light intensity as shown in Figure 2, reflecting on the strong influence that Gr-TMD contacts has on the total resistance of the device. The photocurrent $I_{\text{photo}} = I_{\text{light}} - I_{\text{dark}}$, was extracted from the output characteristics of the devices under dark and illuminated conditions. Shown in Figure 3b, the photocurrent generated from all devices increased with larger applied bias. Under the same irradiation power, the WS_2/MoS_2 bilayer device generated the largest photocurrent compared with TMD bilayer devices, which were then followed by the TMD monolayer devices.

For a photoconductor, photoresponsivity (R), photoconductive gain (G) and specific detectivity (D^*) are important figures of merit used to measure the photoelectrical properties of the device. We now calculate these figures of merit and see how the different types of TMD photoconductors compare using these metrics. Photoresponsivity is defined as $R = \frac{I_{\text{photo}}}{P_{\text{light}}}$, where I_{photo} is the generated photocurrent and P_{light} the incident light power on the semiconducting device. Figure 3c shows the power dependence of R under

11 different light intensity for all five types of devices. The negative correlation of R and light intensity reflects the sub-linear photocurrent generation with increasing irradiation power. This is due to the saturation of trap states under high power illumination and also the shortening of carrier lifetime due to increased self-collision and quenching as more charge carriers populate the conduction band.[22] The TMD bilayers also show larger photoresponse than their monolayer counterparts, which could be due to the following reasons: increased absorbance due to extra layer, lower channel resistivity, increased mobility due to encapsulation of the bottom layer, and introduction of new trap sites following an additional layer transfer. Surprisingly, WS_2/MoS_2 heterobilayer devices are found to exhibit a significantly large photoresponsivity as high as 2340 A/W, which is over 10 times larger than TMD homobilayer devices, and 10^3 factor improvement compared with the TMD monolayer devices (Table 1).

In photoconductors, external photoconductive gain (G_{ext}) is defined as the number of photogenerated charge carriers (either electrons or holes) that are collected at the electrodes divided by the number of incident photons on the photoconductor. We can describe the relationship of external photoconductive gain and photoresponsivity by the following expression:

$$R = G_{\text{ext}} \cdot e/h\upsilon \tag{1}$$

where G_{ext} *is* the external photogain, e the elementary charge unit, h the Planck's constant and υ the incident photon frequency. Considering the absorbed photons of the devices, we can further derive the internal photoconductive gain (G_{int}) using $G_{\text{int}} = {}^{G_{\text{ext}}}/_{QE}$, where QE stands for quantum efficiency, and synonymous with light absorbance in cases of photoconductors. We assume an absorbance of 8% and transmittance of 92% for both MoS_2 and WS_2 monolayers under λ=532 nm light source for the calculation of G_{int}.[4] Specific detectivity (D^*) characterizes a photodetector's sensitivity by taking into account the bandwidth, geometry and noise of the device. It is given by $D^* = \frac{R\times(Af)^{1/2}}{i_{\text{n}}}$, where A is the effective area of the detector, f is the electrical bandwidth, and i_n is the noise current. For a rough estimation of the

sensitivity, we assume that the dark current is dominated by shot noise, which is independent of frequency, D^* can be then expressed as

$$D^* = RA^{1/2}/(2eI_{\mathrm{dark}})^{1/2} \quad (2)$$

where I_{dark} is the measured dark current and A is the effective area of the photoconductor. It should be worth noting that devices based on 2D crystals contain 1/f noise components due to non-ideal contacts and defects which cannot be neglected.[23,24] Table 1 records the highest observed values of the figures of merit of the 5 types of photoconductors in this study. The WS_2/MoS_2 bilayer photodetectors exhibited the highest photoresponsivity of up to 2340 A/W and a large internal photoconductive gain over 3.7×10^4, with an estimated specific detectivity of 4×10^{11} Jones (Jones = cm $Hz^{1/2}$ W^{-1}).

The transient photocurrent response of WS_2/MoS_2 heterobilayer device is shown in Figure 3d exhibiting an ON/OFF ratio (defined as $I_{\mathrm{photo}}/I_{\mathrm{dark}}$) of ~5 under illuminated and dark conditions. The large decay time, which is more than a few seconds, is strong indication of the existence of trapped charges across the heterostructure semiconducting channel.

Device structure	no. of sample	Av. R (A W^{-1})	σ (A W^{-1})	R_{max} (A W^{-1})	G_{ext}	G_{int}	D^* (Jones)
WS_2/MoS_2 bilayer	16	1173	462	2340	5460	37096	4.1×10^{11}
MoS_2 (2L)	5	83	35	120	280	1902	3.5×10^{11}
WS_2 (2L)	10	64	36	93	217	1474	1.7×10^{11}
MoS_2 (1L)	8	2.2	1.1	3.7	8.6	108	1.1×10^{10}
WS_2 (1L)	6	0.8	0.2	1.1	2.6	18	1.5×10^{10}

Table 1. TMD Photoconductors and their figure of merits. Device performance statistics (number of samples measured, average photoresponsivity and standard deviation of result) and highest recorded figure of merits including photoresponsivity, photogain (external and internal), and specific detectivity under ambient conditions (V_{bias}= 10 V, V_g= 0 V, λ=532 nm, P_{light} = 1.7×10^4 mW/cm^2).

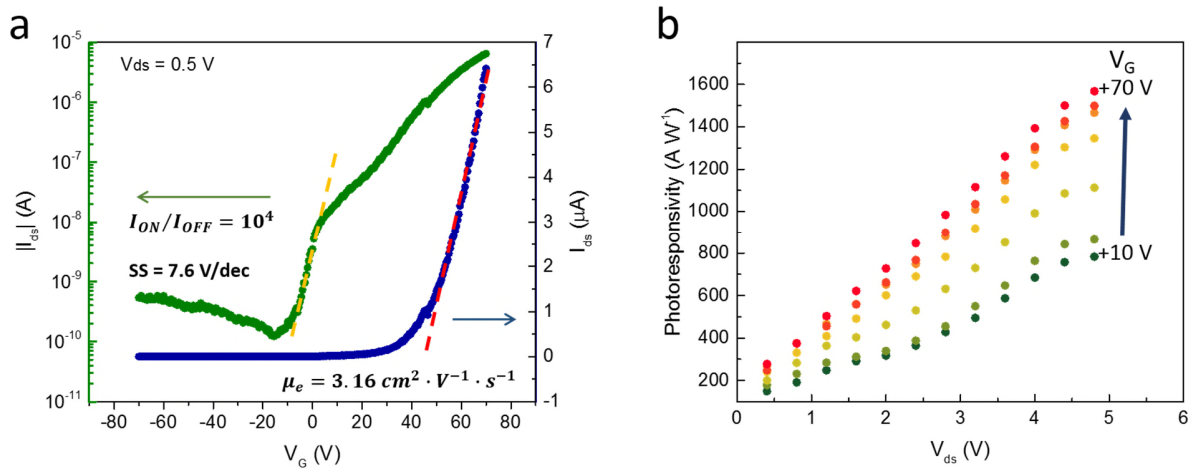

Figure 4. Gate dependence characteristics of a WS_2/MoS_2 bilayer device. (a) I_{ds}-V_g plot of hybrid device on linear scale (blue) and logarithmic scale (green) indicating the N-type characteristic of WS_2/MoS_2 heterostructure. An on/off ratio of 10^4 and subthreshold swing (SS) of 7.6 V/dec are obtained from the logarithmic plot, and electron mobility extracted from the linear region of the transfer curve shows to be 3.16 $cm^2/(V \cdot s)$. (b) Photoresponsivity versus V_{ds} with increasing applied back gate potential under illumination power of 1.7×10^4 mW/cm^2.

Applying gate potential is the most common and effective way to control the behavior of semiconductor devices. In our previous studies[12,25] we find that gate is not only capable of tuning the Fermi level of the semiconducting TMD but can also tune the work function of graphene due to the its limited density of states. As a result, modification the Schottky barrier height at the Gr-TMD interface can be achieved. Here we investigate the gate influences on a graphene contacted WS_2/MoS_2 heterobilayer device. We first perform a gate sweep to the heterobilayer sample to probe its performance as a field-effect transistor. From the transfer curve (Figure 4a) we gather a typical N-type behavior of a WS_2/MoS_2 heterobilayer. The estimated mobility of the hybrid device can be extracted using $\mu = \frac{dI_{ds}}{dV_g} \cdot \frac{L}{w} \cdot \frac{1}{V_{sd}} \cdot \frac{1}{C_{ox}}$, where L and w are the channel's length and width respectively, and C_{ox} is the gate capacitance of the SiO_2 substrate. We obtain an effective mobility of μ = 3.16 cm^2 V s^{-1}. Alongside the I-V_g curve on linear scale (blue curve) is the same data plotted against a logarithmic y-scale (green curve), which shows an ON/OFF ratio as high as 10^5 in the N-type region. The subthreshold swing is calculated from the slope of subthreshold

region (yellow dotted line) to be 7.6 V/dec, which is in a range consistent with previous reports based on CVD-grown TMD.[26,27] This value of subthreshold swing is quite far from the theoretical limit of 60 mV/dec, indicating non-ideality of the contacts and the existence of trapped states.

In Figure 4b we demonstrate that the device photoresponsivity under fixed illumination can be further improved by applying positive gate potential. The photoresponse of our WS_2/MoS_2 heterostructure device under V_{ds}=5 V increases with larger applied positive gate voltage and more than doubles its original value under a gate potential at V_g=+70 V. Our results once again show that Schottky barriers formed between the Gr-TMD are sensitive to photo-illumination and gate potential as is evident in our previous studies,[12,25] and further demonstrates gate modification of Schottky barrier height for optimized device performance of Gr-TMD-Gr photoconductors.

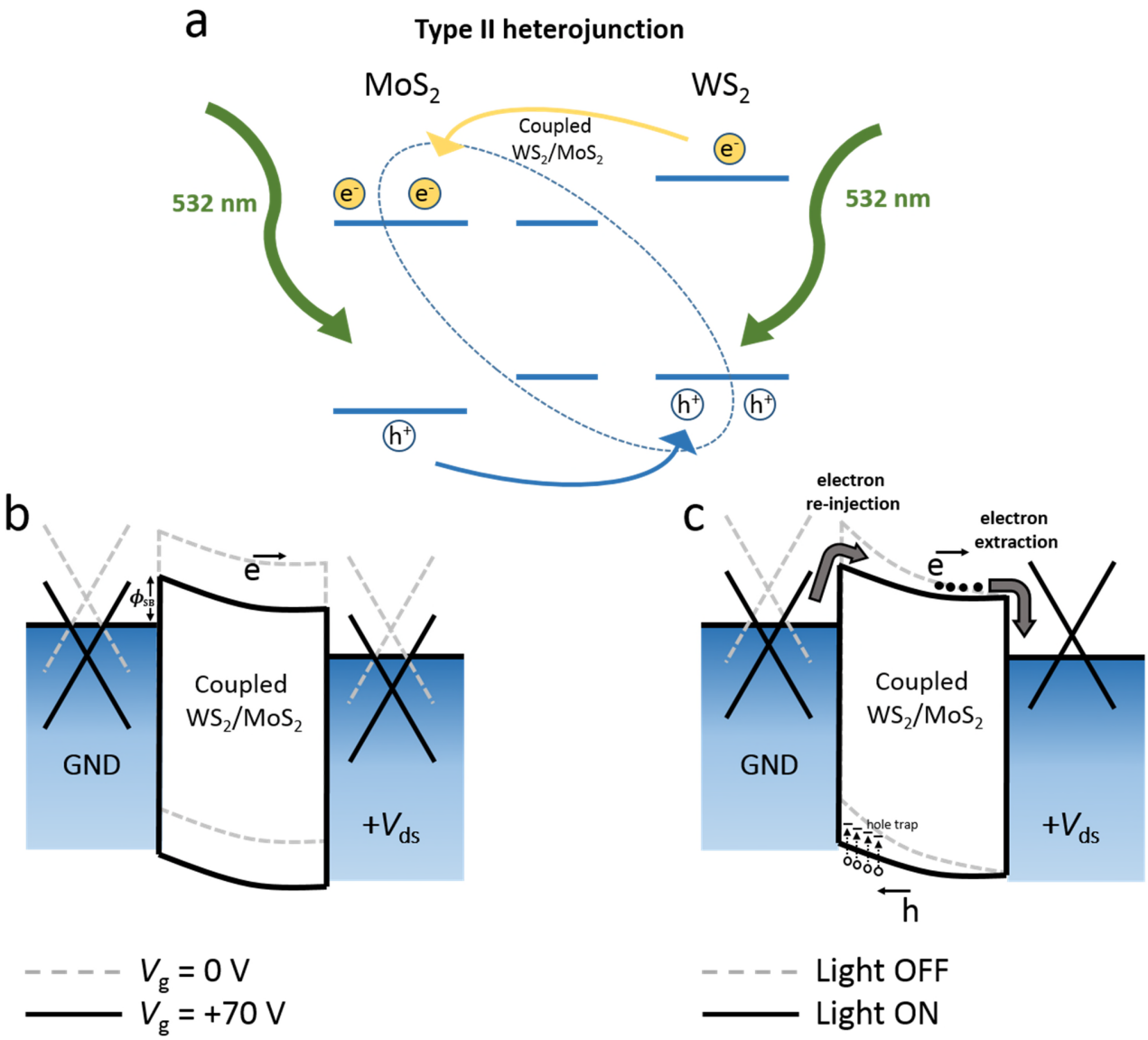

Figure 5. Dynamics of interlayer charge transfer and carrier transportation of Gr-WS_2/MoS_2-Gr photodetector. (a) Band schematic of a vertically stacked WS_2/MoS_2 heterostructure. Due to the type II band alignment, photo-excited electrons and holes tend to accumulate on separate layers. The carrier separation occurs within picoseconds, forming layer-separated excitons with electrons and holes residing at MoS_2 and WS_2 respectively. (b) Band schematic of device while applying positive back-gate potential. Graphene's work function Φ_{Gr} can be tuned by positive gate, leading to lowering of the Schottky barrier at the Gr-TMD interface. (c) Band schematic of device under light irradiation. Upon illumination, formed layer-separated excitons across WS_2 and MoS_2 suppresses electron-hole recombination and further dissociates to free carriers. Under external electric field given by $+V_{ds}$, electrons drift toward the drain electrode which is extracted as photocurrent, while holes drift

towards graphene source electrode connected to ground (GND). Trapped states within the TMD bilayer facilitates an accumulation of holes near the Gr-TMD interface at the source region, creating a positive photogating effect on the graphene electrode and lowers the Schottky barrier at the source. This allows increase in thermionic emission over the Gr-TMD Schottky barrier leading to increased injection of electrons from source electrode to the WS_2/MoS_2 channel, and thus facilitates the circulation of electrons within the photodetector.

To make sense of the improved performance in a WS_2/MoS_2 heterobilayer photodetector, we turn to the dynamics of interlayer coupling between a vertically stacked WS_2 and MoS_2 heterostructure. Figure 5a shows the band schematic of a type II band alignment formed at the WS_2/MoS_2 heterobilayer. Upon illumination, photo-excited electrons and holes prefer to stay at different layers, where the electrons reside at the conduction band of MoS_2 while holes transfer to WS_2 at the interface.[13] The N-type characteristics of the WS_2/MoS_2 heterobilayer device suggests that MoS_2 may act as the main conductive channel in which the majority carrier (electron) transits within a closed circuit.

Figure 5b shows the band diagram of the Gr-WS_2/MoS_2 heterobilayer-Gr device under applied gate. The Dirac cones of graphene band structure results in a work function that is susceptible to gate potential. This implies a gate tunable Schottky barrier, which in this study is determined by the band offset at the metal-semiconductor interface expressed as $\Phi_{SB} = \Phi_{Gr} - \chi_{TMD}$. A positive gate will lower (raise) the work function (Fermi level) of graphene electrodes, and lead to a lowering in Φ_{SB}. Figure 5c shows the band diagram of the device under dark and illuminated conditions. Upon illumination, the recombination of electron-hole pairs is suppressed due to the interlayer charge transfer between WS_2 and MoS_2. Under an applied bias $+V_{ds}$, electrons and holes drift towards opposite sides. The electrons are collected at the drain electrode which contributes to the photocurrent, while with the existence of trap states, holes start to accumulate at the source region. The accumulation of holes at the region acts as a positive gate on the source graphene electrode, in effect raising the Fermi level of the graphene electrode and lowering the Φ_{SB}. This lowering of barrier due to photogating effect will facilitate the re-injection of electrons into the TMD channel. Photoconductors rely on such a mechanism to enable photoconductive gain, where minority carriers are trapped so that majority carriers can recirculate along the channel for each absorbed photon.

The interlayer coupling between WS_2 and MoS_2 may therefore facilitate such a long-lived trap state necessary for large photoconductive gain.[15,20] This may help explain the significantly large photoconductive gain and responsivity that is observed in our graphene contacted WS_2/MoS_2 heterobilayer photoconductors.

Unlike vertical Gr-TMD-Gr photodiodes which limited to photocurrent generation based on photovoltaic mechanisms or tunneling currents,[9,11,21] our lateral photodetector based on WS_2/MoS_2 heterobilayer relies on a photogating mechanism and can thus reach an external quantum efficiency over unity with significant photoresponsivity. The gating effect is made possible due to the suppressed recombination of electron-hole pairs at separated layers of the WS_2/MoS_2 heterostructure, creating free electrons that circulate through the photodetector and holes that act as positive gate. Moreover, the device architecture of a TMD heterobilayer sandwiching graphene electrodes allows a direct contact between metal-semiconductor and enables a more efficient gating effect to take place during irradiation.

Conclusion

In summary, we demonstrated a high-performing lateral MSM photodetector based on graphene-contacted WS_2/MoS_2 heterostacks. Utilizing the efficient interlayer charge transfer between WS_2 and MoS_2, we achieved a photoresponsivity of up to 2340 A/W and an internal photoconductive gain of over 3.7×10^4, improving photoresponsivity by over an order of magnitude compared with the respective TMDs monolayers and bilayers. All the crystals used to fabricate the lateral photodetectors have been synthesized using CVD, eliminating mechanical exfoliation and therefore allowing production of device arrays on a large scale. This demonstration of a high performing hybrid TMD photodetector points to a promising route to optimize photodetectors' performance by controlling interlayer charge transfer between van der Waals crystals.

Experimental Methods

CVD-growth of monolayer Graphene, MoS_2 and WS_2

Monolayer graphene was grown using our previously reported method involving deposition on liquid Cu with tungsten substrate.[28] Graphene was grown on the melted Cu with a flow of 200 standard cubic centimeters per minute (sccm) argon, 30 sccm hydrogen (25%) and 10 sccm of methane (1%) gas for 90 min, subsequently followed by a secondary growth process at 1060 ^{o}C for 30 min. The sample was then removed from the heating zone and cooled to room temperature.

Monolayer MoS_2 was grown on a 300 nm SiO_2/Si substrate using Molybdenum trioxide (MoO_3) and sulfur (S, ≥99.5%, Sigma-Aldrich) powders under atmospheric pressure. Two furnaces were used to individually control the temperature of both precursors. The MoO_3 and sulfur powder were loaded separately in two tubes of different diameters in order to strictly define the reaction region around the substrate surface. Argon was used as the carrier gas with a flow rate of 150 sccm. The S, MoO_3 and SiO_2/Si substrate were heated to 180, 300, and 800 ^{0}C, respectively, and the reaction occurred for 30 min.

Monolayer WS_2 was grown on 300 nm SiO_2/Si substrate using our previously reported method [29] using Tungsten trioxide (WO_3) and sulfur as precursors, but with the addition of hydrogen. The two precursors, WO_3 and sulfur powder are positioned in the internal and external tube respectively within a double-walled-quartz-tube, and heated separately by two furnace systems. The whole system was first flushed with 500 sccm argon gas for 30 minutes, followed by a pre-introduction of sulfur by heating the sulfur powder up to 180 °C. The reaction was conducted under the temperature of 1150 °C for 3 minutes with a hydrogen/argon ratio of 1/19. The as-grown WS_2 samples were fast cooled as soon as the reaction is completed.

Transfer of CVD-grown crystals

The as-grown CVD samples were first spin-coated with a poly(methyl methacrylate) (PMMA) scaffold (8 wt% in anisole, 495k molecular weight). Tungsten substrate of the Graphene sample was electrochemically etched in NaOH (2 M) by connecting a 2.4 V on the sample and using a Cu foil as anode.[30] The PMMA/Graphene film was then separated from Cu substrate by $(NH_4)_2S_2O_8$ etching (0.1 M). The PMMA/MoS_2 and PMMA/WS_2 films were separated from the SiO_2/Si substrate by KOH etching (1 M) at 60 ^oC. The floating films were carefully transferred several times into deionized water for cleansing purposes. The films were subsequently transferred onto Si chip and baked at 150 ^oC for 30 min for sample adhesion. This is then followed by soaking sample in hot acetone of 45 ^oC for PMMA removal.

Device fabrication

JEOL 5500 FS EBL system was used to pattern bond pads in a bilayer PMMA positive resist. A thermal evaporator was used to deposit Au (100 nm) bond pads onto a 300 nm SiO_2/Si substrate, followed by liftoff in hot acetone. Graphene/PMMA film was transferred onto the Si chip with pre-patterned bond pads, and baked overnight at 180 ^oC for better adhesion to substrate. Graphene film was then patterned using EBL with negative resist and oxygen plasma etching to define graphene channels with a length and width of 100 μm and 15 μm respectively. Gaps of 1 μm between graphene channels were fabricated using the same process with positive resist. The Au/Gr contacts were lifted together using PMMA scaffold by etching away the SiO_2 substrate, and transferred onto another piece of Si chip with pre-transferred TMD domains. This is followed by additional transfer of TMD domains using the same method. For TMD heterobilayer devices, WS_2 and MoS_2 are used as bottom and top layers respectively. All bilayer devices measured in this study are bilayer stacks made via the described transfer method, and not as-grown bilayers.

Optoelectronic characterization of devices

Raman and PL spectroscopy was carried out using a LabRam Aramis Raman Spectrometer. Samples are illuminated with a 532 nm laser of 200 μW, through a ×50 objective lens with a spot size of ~2 μm. A Keithley 2400 source meter was used for *I-V* characteristics and responsivity of the Gr-WS_2-Gr photodetectors. For illumination during photoresponse measurements, a 532 nm diode-pumped solid-state laser (Thorlabs, DJ532-40) which was coupled into a confocal microscope to form a beam with spot size radius of ~10 μm as a light source. The power values of the output laser are taken by a manually fixated power meter (Thorslab Optics PM100D, ±3 % accuracy) placed above the devices before each *I-V* measurement. Tungsten tips connected to a Keithley 2400 source meter are used to probe the metal bond-pads of each devices and to apply a bias sweep from -10 V to +10 V.

Supporting Information

The Supporting Information is available free of charge on the ACS Publications website at DOI:

Raman and PL characterization of CVD-grown TMDs. Calculation of effective Schottky barrier height at Gr-TMD interface.

Acknowledgements

J.H.W thanks the support from the Royal Society and Samsung. H. T. thanks Yayasan Khazanah for funding the Merdeka Scholarship.

References

(1) Wang, Q. H.; Kalantar-Zadeh, K.; Kis, A.; Coleman, J. N.; Strano, M. S. Electronics and Optoelectronics of Two-Dimensional Transition Metal Dichalcogenides. *Nat. Nanotechnol.* **2012**, *7*, 699–712.

(2) Jariwala, D.; Sangwan, V. K.; Lauhon, L. J.; Marks, T. J.; Hersam, M. C. Emerging Device Applications for Semiconducting Two-Dimensional Transition Metal Dichalcogenides. *ACS Nano* **2014**, *8*, 1102–1120.

(3) Pospischil, A.; Mueller, T. Optoelectronic Devices Based on Atomically Thin Transition Metal Dichalcogenides. *Applied Sciences*, **2016**, *6*, 78.

(4) Bernardi, M.; Palummo, M.; Grossman, J. C. Extraordinary Sunlight Absorption and One Nanometer Thick Photovoltaics Using Two-Dimensional Monolayer Materials. *Nano Lett.* **2013**, *13*, 3664–3670.

(5) Geim, A. K.; Grigorieva, I. V. Van Der Waals Heterostructures. *Nature* **2013**, *499*, 419–425.

(6) Withers, F.; Del Pozo-Zamudio, O.; Mishchenko, A.; Rooney, A. P.; Gholinia, A.; Watanabe, K.; Taniguchi, T.; Haigh, S. J.; Geim, A. K.; Tartakovskii, A. I.; Novoselov, K. S. Light-Emitting Diodes by Band-Structure Engineering in van Der Waals Heterostructures. *Nat Mater* **2015**, *14*, 301–306.

(7) Cheng, R.; Li, D.; Zhou, H.; Wang, C.; Yin, A.; Jiang, S.; Liu, Y.; Chen, Y.; Huang, Y.; Duan, X. Electroluminescence and Photocurrent Generation from Atomically Sharp WSe2/MoS2 Heterojunction P–N Diodes. *Nano Lett.* **2014**, *14*, 5590–5597.

(8) Lee, C.-H.; Lee, G.-H.; van der Zande, A. M.; Chen, W.; Li, Y.; Han, M.; Cui, X.; Arefe, G.; Nuckolls, C.; Heinz, T. F.; Guo, J.; Hone, J.; Kim, P. Atomically Thin P–N Junctions with van Der Waals Heterointerfaces. *Nat. Nanotechnol.* **2014**, *9*, 676–681.

(9) Furchi, M. M.; Pospischil, A.; Libisch, F.; Burgdörfer, J.; Mueller, T. Photovoltaic Effect in an Electrically Tunable van Der Waals Heterojunction. *Nano Lett.* **2014**, *14*, 4785–4791.

(10) Zhang, K.; Zhang, T.; Cheng, G.; Li, T.; Wang, S.; Wei, W.; Zhou, X.; Yu, W.; Sun, Y.; Wang, P.; Zhang, D.; Zeng, C.; Wang, X.; Hu, W.; Fan, H. J.; Shen, G.; Chen, X.; Duan, X.; Chang, K.;

Dai, N. Interlayer Transition and Infrared Photodetection in Atomically Thin Type-II MoTe2/MoS2 van Der Waals Heterostructures. *ACS Nano* **2016**, *10*, 3852–3858.

(11) Britnell, L.; Ribeiro, R. M.; Eckmann, A.; Jalil, R.; Belle, B. D.; Mishchenko, A.; Kim, Y.-J.; Gorbachev, R. V; Georgiou, T.; Morozov, S. V; Grigorenko, A. N.; Geim, A. K.; Casiraghi, C.; Neto, A. H. C.; Novoselov, K. S. Strong Light-Matter Interactions in Heterostructures of Atomically Thin Films. *Science* **2013**, *340*, 1311-1314.

(12) Tan, H.; Fan, Y.; Zhou, Y.; Chen, Q.; Xu, W.; Warner, J. H. Ultrathin 2D Photodetectors Utilizing Chemical Vapor Deposition Grown WS2 With Graphene Electrodes. *ACS Nano* **2016**, *10*, 7866–7873.

(13) Hong, X.; Kim, J.; Shi, S.-F.; Zhang, Y.; Jin, C.; Sun, Y.; Tongay, S.; Wu, J.; Zhang, Y.; Wang, F. Ultrafast Charge Transfer in Atomically Thin MoS2/WS2 Heterostructures. *Nat. Nanotechnol.* **2014**, *9*, 682–686.

(14) Chen, H.; Wen, X.; Zhang, J.; Wu, T.; Gong, Y.; Zhang, X.; Yuan, J.; Yi, C.; Lou, J.; Ajayan, P. M.; Zhuang, W.; Zhang, G.; Zheng, J. Ultrafast Formation of Interlayer Hot Excitons in Atomically Thin MoS2/WS2 Heterostructures. *Nat. Commun.* **2016**, *7*, 12512.

(15) Rivera, P.; Schaibley, J. R.; Jones, A. M.; Ross, J. S.; Wu, S.; Aivazian, G.; Klement, P.; Seyler, K.; Clark, G.; Ghimire, N. J.; Yan, J.; Mandrus, D. G.; Yao, W.; Xu, X. Observation of Long-Lived Interlayer Excitons in Monolayer MoSe2–WSe2 Heterostructures. *Nat. Commun.* **2015**, 6, 6242.

(16) Yuan, J.; Najmaei, S.; Zhang, Z.; Zhang, J.; Lei, S.; M Ajayan, P.; Yakobson, B. I.; Lou, J. Photoluminescence Quenching and Charge Transfer in Artificial Heterostacks of Monolayer Transition Metal Dichalcogenides and Few-Layer Black Phosphorus. *ACS Nano* **2015**, *9*, 555–563.

(17) Fang, H.; Battaglia, C.; Carraro, C.; Nemsak, S.; Ozdol, B.; Kang, J. S.; Bechtel, H. A.; Desai, S. B.; Kronast, F.; Unal, A. A.; Conti, G.; Conlon, C.; Palsson, G. K.; Martin, M. C.; Minor, A. M.; Fadley, C. S.; Yablonovitch, E.; Maboudian, R.; Javey, A. Strong Interlayer Coupling in van Der Waals Heterostructures Built from Single-Layer Chalcogenides. *Proc. Natl. Acad. Sci.* **2014**, *111*, 6198–6202.

(18) Tongay, S.; Fan, W.; Kang, J.; Park, J.; Koldemir, U.; Suh, J.; Narang, D. S.; Liu, K.; Ji, J.; Li, J.; Sinclair, R.; Wu, J. Tuning Interlayer Coupling in Large-Area Heterostructures with CVD-Grown MoS2 and WS2 Monolayers. *Nano Lett.* **2014**, *14*, 3185–3190.

(19) Chen, H.; Wen, X.; Zhang, J.; Wu, T.; Gong, Y.; Zhang, X.; Yuan, J.; Yi, C.; Lou, J.; Ajayan, P. M.; Zhuang, W.; Zhang, G.; Zheng, J. Ultrafast Formation of Interlayer Hot Excitons in Atomically Thin MoS2/WS2 Heterostructures. *Nat. Commun.* **2016**, *7*, 1–8.

(20) Palummo, M.; Bernardi, M.; Grossman, J. C. Exciton Radiative Lifetimes in Two-Dimensional Transition Metal Dichalcogenides. *Nano Lett.* **2015**, *15*, 2794–2800.

(21) Yu, W. J.; Liu, Y.; Zhou, H.; Yin, A.; Li, Z.; Huang, Y.; Duan, X. Highly Efficient Gate-Tunable Photocurrent Generation in Vertical Heterostructures of Layered Materials. *Nat. Nanotechnol.* **2013**, *8*, 952–958.

(22) Liu, F.; Shimotani, H.; Shang, H.; Kanagasekaran, T.; Zólyomi, V.; Drummond, N.; Fal'ko, V. I.; Tanigaki, K. High-Sensitivity Photodetectors Based on Multilayer GaTe Flakes. *ACS Nano* **2014**, *8*, 752–760.

(23) Kufer, D.; Konstantatos, G. Highly Sensitive, Encapsulated MoS2 Photodetector with Gate Controllable Gain and Speed. *Nano Lett.* **2015**, *15*, 7307–7313.

(24) Kwon, H.-J.; Kang, H.; Jang, J.; Kim, S.; Grigoropoulos, C. P. Analysis of Flicker Noise in Two-Dimensional Multilayer MoS2 Transistors. *Appl. Phys. Lett.* **2014**, *104*, 83110.

(25) Tan, H.; Fan, Y.; Rong, Y.; Porter, B.; Lau, C. S.; Zhou, Y.; He, Z.; Wang, S.; Bhaskaran, H.; Warner, J. H. Doping Graphene Transistors Using Vertical Stacked Monolayer WS2 Heterostructures Grown by Chemical Vapor Deposition. *ACS Appl. Mater. Interfaces* **2016**, 8, 1644-1652.

(26) Fan, Y.; Zhou, Y.; Wang, X.; Tan, H.; Rong, Y.; Warner, J. H. Photoinduced Schottky Barrier Lowering in 2D Monolayer WS $_2$ Photodetectors. *Adv. Opt. Mater.* **2016**, *4*, 1573–1581.

(27) Lan, C.; Li, C.; Yin, Y.; Liu, Y. Large-Area Synthesis of Monolayer WS2 and Its Ambient-Sensitive Photo-Detecting Performance. *Nanoscale* **2015**, *7*, 5974–5980.

(28) Wu, Y. A.; Fan, Y.; Speller, S.; Creeth, G. L.; Sadowski, J. T.; He, K.; Robertson, A. W.; Allen, C. S.; Warner, J. H. Large Single Crystals of Graphene on Melted Copper Using Chemical Vapor Deposition. *ACS Nano* **2012**, *6*, 5010–5017.

(29) Rong, Y.; Fan, Y.; Koh, A. L.; Robertson, A. W.; He, K.; Wang, S.; Tan, H.; Sinclair, R.; Warner, J. H. Controlling Sulphur Precursor Addition for Large Single Crystal Domains of WS2. *Nanoscale* **2014**, *6*, 12096–12103.

(30) Fan, Y.; He, K.; Tan, H.; Speller, S.; Warner, J. H. Crack-Free Growth and Transfer of Continuous Monolayer Graphene Grown on Melted Copper. *Chem. Mater.* **2014**, *26*, 4984–4991.

TOC